A Highly Magnetic Integrated Method of *LCC*-Compensated IPT System With Excellent Misalignment Tolerance

Ke Shi, Tianxu Feng, Jincheng Jiang, Peiyue Wang, Zhenya Meng, and Chunsen Tang, *Member, IEEE*

***Abstract*—Compactness and effectiveness are two basic considerations of the inductive power transfer (IPT) system. This article proposes a highly magnetic integrated method of *LCC*-compensated IPT system in which coupling coils are integrated into the coupler to improve the misalignment tolerance and realize the design of zero-voltage switching (ZVS) condition. The primary-side coupler integrates a double-layer reverse coil and an inductor coil in the *LCC* resonant network to improve misalignment tolerance and compactness. The secondary-side coupler integrates an inductor coil in the *LCC* resonant network to realize the ZVS condition. The main advantage is that extra space and magnetic cores for the external compensation inductors are saved, accompanied by excellent misalignment tolerance and ZVS parameter configuration. And output power stability under misalignment with fewer mutual inductance cancel sacrifices is realized. A detailed design method of the coupler is given based on the circuit analysis. A 3-kW power level prototype is implemented to validate the proposed design. Experimental results show that the IPT system with the proposed design can retain the well-aligned power at 40% misalignment. The mutual inductance cancellation caused by the reverse coil is reduced to 51%, and the efficiency reaches 93.1%.**

***Index Terms*—Inductive power transfer (IPT), integrated magnetic coupler, *LCC* compensation, misalignment, reverse coil.**

I. Introduction

With the rapid growth of population and economy, traditional energy shortages and environmental pollution problems have become increasingly prominent. The inductive power transfer (IPT) system has proven to be an effective solution with features such as avoiding bulky cables, availability of galvanic isolation, more freedom of operation, weatherproofing, low maintenance, and higher safety. It has been widely used in biomedical implants [1], consumer electronics [2], and electric vehicles [3], [4], [5].

IPT systems eliminate the shackles of physical media, giving the transmitter and receiver considerable flexibility. However, the independence of mechanical structure makes it difficult to ensure complete alignment. The misalignments cause a variation in the mutual inductance between the coupling coils, resulting in a reduction in the transferred power, instability, and more power losses. Therefore, misalignment tolerance is an important performance index of the IPT systems.

Based on previous studies, the misalignment tolerance improvement of IPT systems is mainly studied from the following three aspects. The first one is to reduce the variation of the mutual inductance between the transmitting and receiving coil by changing the shape of the magnetic coupler [6], [7], [8]. The focus of these methods is to achieve a single stable coupling for power transfer through the design of the coil shape, magnetic core structure, coil polarity, and winding method. The second one is to employ control schemes to match the mutual inductance under misalignment [9], [10], [3]. The extra control modules increase the complexity of the IPT system, and the customization requirements for different systems weaken the versatility. The third one is to design the compensation topology and parameters to achieve stable transferred power under variation of mutual inductance [11], [12], [13]. The constant output current characteristics are changed in the parameter configuration of these methods. And since the coupling channel is not essentially changed, the performance of the misalignment tolerance is limited.

The *LCC* compensation topology has been widely adopted because it provides power proportional to the coupling coefficient and achieves a constant output current operating mode for battery charging applications [14]. However, more inductor components are required, increasing the complexity of the system. The external compensation inductor has problems such as occupying more space, difficult heat dissipation, and more magnetic cores used. In addition, it hinders the modularization of wireless power transmission equipment.

To save the space required by the extra inductor and solve the problem of the bulky space occupied by the resonant network, Li et al. [15] first integrated the compensation coil into

---

Manuscript received 7 June 2023; revised 28 July 2023; accepted 2 September 2023. Date of publication 5 September 2023; date of current version 23 October 2023. This work was supported in part by the National Key Research and Development Program of China under Grant 2022YFE0204500, in part by the National Natural Science Foundation of China under Grant 52277002, and in part by the Natural Science Foundation Postdoctoral Science Foundation Project of Chongqing under Grants cstc2021jcyj-bshX0245 and cstc2021jcyj-bshX0159. Recommended for publication by Associate Editor J. Acero. *(Corresponding author: Ke Shi.)*

Ke Shi, Tianxu Feng, Jincheng Jiang, Peiyue Wang, and Zhenya Meng are with the School of Automation, Chongqing University of Posts and Telecommunications, Chongqing 400065, China (e-mail: shike@cqupt.edu.cn; fengtx@cqupt.edu.cn; jiangjinc@cqupt.edu.cn; wangpy@cqupt.edu.cn; mengzy@cqupt.edu.cn).

Chunsen Tang is with the School of Automation, Chongqing University, Chongqing 400000, China (e-mail: cstang@cqu.edu.cn).

Color versions of one or more figures in this article are available at https://doi.org/10.1109/TPEL.2023.3312215.

Digital Object Identifier 10.1109/TPEL.2023.3312215

the magnetic coupler. In the preliminary research stage of the magnetic integrated coupler, the additional coupling caused by the integrated coil is expected to be weakened or even eliminated. The integrated decoupled resonant inductor coil was proposed to improve the compactness of the magnetic coupler [16], [17]. Later, the cross-coupling properties due to magnetic integration were further investigated and applied to improve the antimisalignment performance [18], [19]. These characteristics were also applied to the electric vehicle dynamic wireless charging system with a short-individual structure to suppress the power fluctuation [20], [21]. The magnetic integrated method provides a reasonable destination for the inductor components required by the *LCC* topology. In addition to the magnetic integration of the compensation inductor in the resonant network, the magnetic integration of the reverse coil was proven to mitigate the mutual inductance variation against the charging distance or misalignment for IPT systems. In [22], a design approach that uses antiparallel resonant loops for IPT systems was presented. An antiparallel resonant structure was formed by forward and reverse loops to stabilize the transfer efficiency under dramatic distance-related changes. In [23], a distance-insensitive wireless power transmission system was designed using a reverse coil. These methods are preliminary explorations of reverse coils, and their focus is to improve vertical distance antimisalignment ability. In [24], the magnetic field strength in some areas was reduced by the reverse loop to suppress electromagnetic interference noise. In [25], the proposed multiple-antiparallel square spiral coils effectively enhanced the height of the charging plane with a uniform magnetic field. In [26], extra forward and reverse loops were added to the existing coils to achieve uniform mutual inductance. In [27], the integrated reverse coil was proposed to improve the antimisalignment performance of the IPT system. Focusing on specific misalignment problems, integrated reverse coils had proven to convert the single mutual inductance coupling mode into the mutual inductance difference coupling mode, thus making the magnetic field distribution more uniform [28], [29], [30]. Although these methods can improve horizontal misalignment tolerance, there is still a defect. The introduction of reverse coils greatly cancels the mutual inductance for power transmission, which is detrimental to the system output power capability and efficiency performance. This article proposed a novel compact solution for the IPT system based on magnetic integration, with excellent misalignment tolerance and a zero-voltage switching (ZVS) working condition configuration. The coupling coils are integrated into the coupler and make sense in three aspects. The integrated double-layer reverse coil on the primary side is to achieve better misalignment characteristics with high efficiency. The integrated inductor coil on the secondary side aims to realize the ZVS condition configuration, which keeps the output power and misalignment characteristics unaffected. The integrated inductor coil on the primary side is to achieve decoupling from other unipolar coils compatible with multidirection misalignments, which improves compactness without affecting the characteristics. All inductors in the *LCC* resonant network and the reverse coil are integrated to form a highly integrated (HI) magnetic coupler. The contributions of this article include the following.

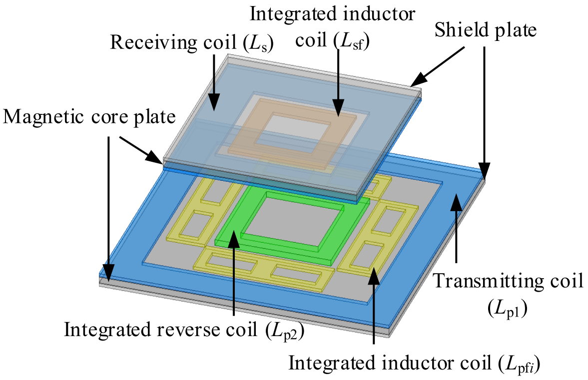

Fig. 1. Proposed HI magnetic coupler.

1) A magnetic coupler that integrates all compensation devices and has excellent antimisalignment performance is presented. The tricky issue of magnetic coupler combined with misalignment tolerance, compactness, and high efficiency is solved, and the performance is optimized.
2) The relationship between the variation rule of total equivalent mutual inductance under misalignment and the geometric size of the reverse coil is clarified. And a double-layer integrated reverse coil structure is proposed to reduce mutual inductance cancellation. Achieving output power stability at 40% misalignment with only 51% mutual inductance sacrifice is realized.
3) The functional relationship between the input impedance phase angle and the mutual inductance produced by the integrated inductor coil and the transmitting coils is derived. The design method of the integrated inductor coil is proposed based on the expression, and better ZVS working conditions are realized.

The rest of this article is organized as follows. In Section II, the HI magnetic coupler is proposed. Based on circuit analysis, the system characteristics and the influence of coupling coils are studied and presented. In Section III, the coupling variation characteristics of the integrated reverse coil under misalignment are analyzed. In Section IV, the quantitative optimization design process of the HI magnetic coupler is given based on the qualitative mutual inductance analysis in Section III. In Section V, the practical system is built and the effectiveness of the proposed method is verified. In Section VI, the output power capability is discussed. Finally, Section VII concludes this article.

II. SYSTEM DESCRIPTION AND CHARACTERISTICS ANALYSIS

A. *Highly Integrated Magnetic Coupler*

The proposed HI magnetic coupler is shown in Fig. 1. The coupler includes a transmitting pad and a receiving pad. Each pad consists of three layers. In the transmitting pad, three coils are placed on the top layer as the transmitting coil, the integrated reverse coil, and the integrated inductor coil in the primary-side *LCC* topology. The magnetic core plate serves as the second layer to enhance the coupling, and the shield plate serves as the bottom layer to reduce electromagnetic leakage. In the receiving

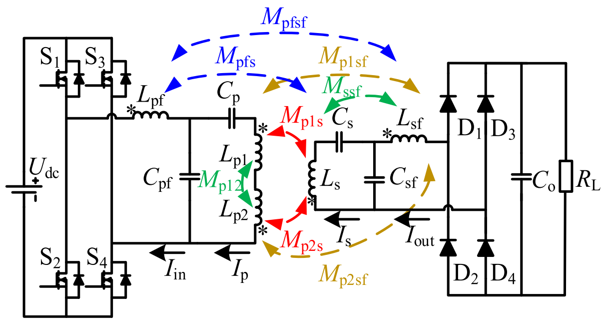

Fig. 2. Circuit topology of IPT system with HI magnetic coupler.

pad, two coils are placed on the top layer as the receiving coil and the integrated inductor coil in the secondary-side *LCC* topology. Similarly, the magnetic core plate and the shield plate are placed on the lower two layers.

The proposed method intends to improve the misalignment tolerance in the *x*-direction and *y*-direction and realizes the full integration of the *LCC*-compensated IPT system. Three integrated coils share the magnetic core and the space in the layer with the main coils, which greatly improves the compactness of the coupler. First, the coupling variation characteristics are changed through the integrated reverse coil, which is used to obtain the equivalent mutual inductance difference to replace the original single coupling. Second, the secondary-side integrated inductor coil introduces a design variable to obtain the desired inverter output phase angle to ensure the ZVS condition. Third, the primary-side integrated inductor coil can be decoupled from other coils when misaligned and well-aligned, making the full magnetic integration more feasible.

B. Circuit Modeling

The circuit topology of IPT systems with an HI magnetic coupler is shown in Fig. 2. U_{dc} is the voltage of the dc power supply. The voltage-fed inverter is composed of MOSFETs S_1–S_4. L_{pf} and L_{sf} are integrated coils that serve as primary-side and secondary-side compensation inductors, respectively. L_{p1} and L_{s} are the transmitting coil and the receiving coil, respectively. L_{p2} is the integrated coil connected in reverse series with the transmitting coil. M_{pfs}, M_{pfsf}, M_{p12}, M_{p1s}, M_{p2s}, M_{p1sf}, M_{p2sf}, and M_{ssf} are eight significant coupling mutual inductances in the system. M_{pfsf} and M_{pfs} can be designed to be ignorable small values relative to the impedance of the components by the coupler proposed in this article. The detailed design is performed in Section III. C_{pf}, C_{p}, C_{s}, and C_{sf} are the capacitors in the *LCC* compensation network, which can be made into boards and easily integrated into the coupler. C_{o} is the filter capacitor. R_{L} is the equivalent load. And the rectifier is composed of diodes D_1–D_4. I_{in} and I_{p} are the inverter current vector and the transmitting coil current vector, respectively. I_{s} and I_{out} are the receiving coil current vector and the output current vector, respectively. The operating frequency of the system is f and the angular frequency is $\omega = 2\pi f$.

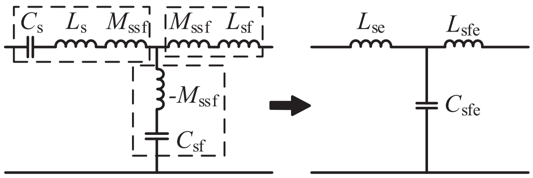

Fig. 3. Equivalent of the same-side internal mutual inductance.

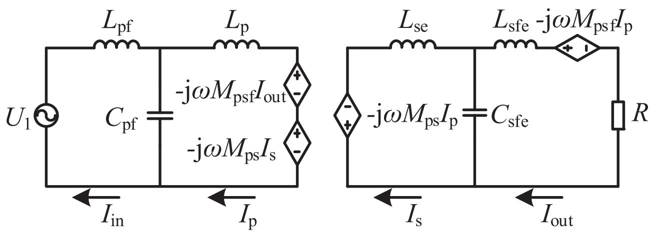

Fig. 4. Equivalent circuit of the topology with HI magnetic coupler.

To be more concise and make the calculation process simplified, the corresponding mutual inductances are defined as

$$M_{\mathrm{ps}} = M_{\mathrm{p1s}} - M_{\mathrm{p2s}}, M_{\mathrm{psf}} = M_{\mathrm{p1sf}} - M_{\mathrm{p2sf}}. \tag{1}$$

M_{ssf} is the same-side internal mutual inductance, which can be equivalent to a T-type network, as shown in Fig. 3. Lumped together as part of the compensated *LCC* network, it can be decoupled as follows:

$$\begin{aligned} L_{\mathrm{se}} &= L_{\mathrm{s}} + M_{\mathrm{ssf}} - \frac{1}{\omega^2 C_{\mathrm{s}}} \\ L_{\mathrm{sfe}} &= L_{\mathrm{sf}} + M_{\mathrm{ssf}} \\ C_{\mathrm{sfe}} &= \frac{C_{\mathrm{sf}}}{1 + \omega^2 M_{\mathrm{ssf}} C_{\mathrm{sf}}}. \end{aligned} \tag{2}$$

Also, M_{p12} is the same-side internal mutual inductance and can be decoupled by

$$L_{\mathrm{p}} = L_{\mathrm{p1}} + L_{\mathrm{p2}} - 2M_{\mathrm{p12}} - \frac{1}{\omega^2 C_{\mathrm{p}}}. \tag{3}$$

Furthermore, the equivalent circuit of the proposed IPT topology with HI magnetic coupler is obtained based on the fundamental harmonics approximation method, as shown in Fig. 4. The square-wave voltages are approximated as sinusoidal sources U_1. The rectifier and the resistance load can be equivalent together to $R_{\mathrm{e}} = 8R_{\mathrm{L}}/\pi^2$. The couplings in the circuit are represented by dependent sources. Focusing on the theoretical feasibility analysis of the proposed method, the power losses of the components are neglected.

The resonant relationship is configured as

$$\omega^2 L_{\mathrm{pf}} C_{\mathrm{pf}} = \omega^2 L_{\mathrm{p}} C_{\mathrm{pf}} = \omega^2 L_{\mathrm{se}} C_{\mathrm{sfe}} = \omega^2 L_{\mathrm{sfe}} C_{\mathrm{sfe}} = 1. \tag{4}$$

By Kirchhoff's laws, the equation describing the system is obtained as

$$\begin{bmatrix} 0 & \mathrm{j}\omega L_{\mathrm{pf}} & 0 & 0 \\ \mathrm{j}\omega L_{\mathrm{pf}} & 0 & -\mathrm{j}\omega M_{\mathrm{ps}} & -\mathrm{j}\omega M_{\mathrm{psf}} \\ 0 & -\mathrm{j}\omega M_{\mathrm{ps}} & 0 & \mathrm{j}\omega L_{\mathrm{se}} \\ 0 & -\mathrm{j}\omega M_{\mathrm{psf}} & \mathrm{j}\omega L_{\mathrm{se}} & R_{\mathrm{e}} \end{bmatrix} \cdot \begin{bmatrix} \dot{I}_{\mathrm{in}} \\ \dot{I}_{\mathrm{p}} \\ \dot{I}_{\mathrm{s}} \\ \dot{I}_{\mathrm{out}} \end{bmatrix} = \begin{bmatrix} \dot{U}_1 \\ 0 \\ 0 \\ 0 \end{bmatrix}. \tag{5}$$

Therefore, the values of the currents are

$$\left|\dot{I}_{\mathrm{p}}\right| = \frac{\left|\dot{U}_1\right|}{\omega L_{\mathrm{pf}}}, \quad \left|\dot{I}_{\mathrm{out}}\right| = \frac{M_{\mathrm{ps}}\left|\dot{U}_1\right|}{\omega L_{\mathrm{pf}} L_{\mathrm{se}}}. \tag{6}$$

From (6), I_{p} and I_{out} are irrelevant to the load, so the system possesses a constant current output characteristic. The output power is expressed as

$$P_{\mathrm{out}} = \left|\dot{I}_{\mathrm{out}}\right|^2 R_{\mathrm{e}} = K_1 M_{\mathrm{ps}}^2 \left|\dot{U}_1\right|^2 R_{\mathrm{e}} \tag{7}$$

where $K_1 = 1/(\omega^2 L_{\mathrm{pf}}^2 L_{\mathrm{se}}^2)$.

In (7), K_1 is determined by the designed system parameters and does not change under misalignment. Thus, the misalignment performance depends on the square of M_{ps}. The result of mathematical derivation in (7) is compatible with the single coupling mode, and the essence of power transmission has not changed. For the usual single-coupled IPT system, the ability to improve the misalignment tolerance through the design of the coupler is limited. In contrast, the mutual difference M_{ps} is expected to achieve a stable output power under misalignment. In this article, the integrated reverse coil is designed in detail to optimize the stability of M_{ps}.

Furthermore, the system input impedance is calculated as

$$Z_{\mathrm{in}} = \frac{\dot{U}_1}{\dot{I}_{\mathrm{in}}} = \frac{\omega^2 L_{\mathrm{pf}}^2 L_{\mathrm{se}}^2}{M_{\mathrm{ps}}\left(M_{\mathrm{ps}} R_{\mathrm{e}} - 2\mathrm{j}\omega L_{\mathrm{se}} M_{\mathrm{psf}}\right)}. \tag{8}$$

Define the ratio of M_{psf} to M_{ps} as ε. Furthermore, the tangent value of the phase angle between the inverter voltage and the inverter current is expressed as

$$\tan\alpha = \frac{\mathrm{Im}[Z_{\mathrm{in}}]}{\mathrm{Re}[Z_{\mathrm{in}}]} = \frac{2\omega L_{\mathrm{se}}\varepsilon}{R_{\mathrm{e}}}. \tag{9}$$

The phase angle α reflects the resonance state of the system. Under the commonly used control strategy of the 50% duty cycle, the ZVS working condition is closely related to the phase angle between the inverter output voltage and current. The positive and negative values of α represent the inductive and capacitive, respectively. In addition, its absolute value represents the degree to which the system deviates from the resonance point. Through ε, the resonance state of the IPT system can be quantified. Based on designed M_{ps} parameters, the normal output power and ZVS working state can be achieved through a reasonable configuration of M_{psf}.

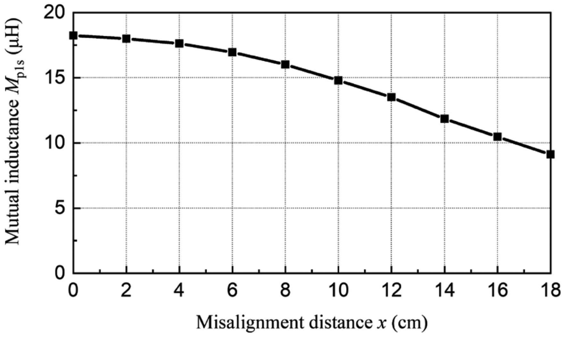

Fig. 5. Variation curve of the mutual inductance M_{p1s} from well-aligned to a 180 mm (40%) misalignment.

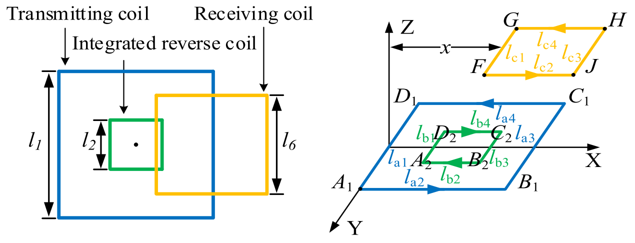

(a) (b)

Fig. 6. Coil structure definition of the coupler. (a) Top view. (b) 3-D view.

III. ANALYSIS OF THE MUTUAL INDUCTANCE

Fig. 5 shows a typical variation curve of the mutual inductance M_{p1s} from well-aligned to a 180 mm (40%) misalignment. From the well-aligned condition to a 40% misalignment, the mutual inductance dropped by nearly 40%. For IPT systems with single mutual inductance for power transfer, it is hard to essentially improve the misalignment performance through the parameter design of the magnetic coupler. Therefore, the primary-side integrated reverse coil is considered to shape the coupling for power transfer to improve the misalignment performance. Theoretically, the variation rule of mutual inductance generated by the integrated reverse coil is expected to be the same as that generated by the transmitting coil. In this way, the equivalent mutual inductance obtained by the superposition of the two couplings can be maintained sufficiently stable under misalignment. The position, size, and turns play a crucial role in the design of integrated reverse coils. Considering the need for system misalignment performance symmetry, the position of the integrated reverse coil should be placed symmetrically at the center of the primary coil. In this section, the influence of size and turns on M_{ps} is analyzed.

Fig. 6 shows the schematic diagram of the coupling coils. The integrated reverse coil is designed inside the transmitting coil and they are center-symmetrical. Each side with multiple turns in the coil has its equivalent position indicated by the middle line. The corresponding parameters are marked in Fig. 6(b). The four sides of the transmitting coil are $l_{\mathrm{a}i}(i = 1, 2, 3, 4)$. The four sides of the integrated reverse coil are $l_{\mathrm{b}j}(j = 1, 2, 3, 4)$. And the four sides of the receiving coil are $l_{\mathrm{c}v}(v = 1, 2, 3, 4)$. The

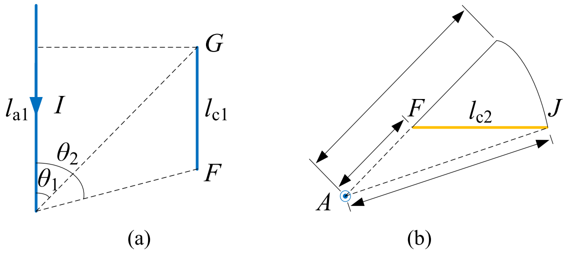

(a) (b)

Fig. 7. Analysis of magnetic flux density. (a) Mean value of magnetic flux density on l_{c1}. (b) Magnetic flux through the receiving coil.

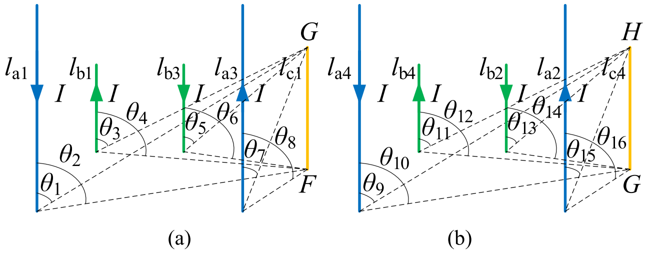

(a) (b)

Fig. 8. Definition of mutual inductance between primary-side coils and the receiving coil. (a) Angle definition from l_{a1}, l_{b1}, l_{b3}, l_{a3} to l_{c1}. (b) Angle definition from l_{a4}, l_{b4}, l_{b2}, l_{a2} to l_{c4}.

endpoints of the coils are marked for definition. Among them, A_1, B_1, C_1, and D_1 are the four endpoints of the transmitting coil. A_2, B_2, C_2, and D_2 are the four endpoints of the integrated reverse coil. F, G, H, and J are four endpoints of the receiving coil. Considering l_{c1} and l_{a1} are parallel, the vertical distance from any point on l_{c1} to l_{a1} is equal, defined as r.

The analysis of the magnetic flux density is shown in Fig. 7. The magnetic field intensity generated by l_{a1} at point F is

$$\vec{B}=\frac{\mu_0 n_{w1} I \vec{e}_\alpha}{4\pi r}\left[\cos\theta_1+\cos\left(\tan^{-1}\frac{r}{l_1-r\cot\theta_1}\right)\right]. \tag{10}$$

Q_1 is the distance from F to A. Q_2 is the superposition of the length of l_{c2} and Q_1. In Fig. 7(a), the mean value of magnetic flux density on l_{c1} is calculated by integral as

$$\begin{aligned}\bar{B}&=\frac{\int_{\theta_1}^{\theta_2} f(\theta)\cdot d\theta}{\theta_2-\theta_1}=\frac{\int_{\theta_1}^{\theta_2}\vec{B}\cdot d\theta}{\theta_2-\theta_1}=\frac{\mu_0 n_{w1} I}{4\pi r(\theta_2-\theta_1)}\\&\quad\times\int_{\theta_1}^{\theta_2}\left(\cos\theta+\cos\left(\tan^{-1}\frac{r}{l_1-r\cot\theta}\right)\right)\cdot d\theta.\end{aligned} \tag{11}$$

The magnetic flux produced by l_{a1} at the receiving coil L_s is

$$\begin{aligned}\boldsymbol{\Phi}&=\iint_S \vec{B}\cdot \mathrm{d}\vec{S}=\int_{|A_1F|}^{|A_1J|}\frac{\mu_0 n_{w1} l_6 I}{4\pi r(\theta_2-\theta_1)}\\&\quad\times\int_{\theta_1}^{\theta_2}\left(\cos\theta+\cos\left(\tan^{-1}\frac{x}{l_1-\frac{x}{\tan\theta}}\right)\right)\mathrm{d}\theta\mathrm{d}r.\end{aligned} \tag{12}$$

The mutual inductance between l_{a1} and L_s is obtained as

$$\begin{aligned}M_{l_{a1}L_s}&=\frac{n_{w4}\boldsymbol{\Phi}}{I}=\frac{\mu_0 l_6 n_{w1} n_{w4}}{4\pi(\theta_2-\theta_1)}\ln\frac{|A_1J|}{|A_1F|}\\&\quad\times\int_{\theta_1}^{\theta_2}\left(\cos\theta+\cos\left(\tan^{-1}\frac{x}{l_{a1}-\frac{x}{\tan\theta}}\right)\right)\mathrm{d}\theta.\end{aligned} \tag{13}$$

Similarly, to obtain the mutual inductances between the other sides and the receiving coil, the relevant angles are defined in Fig. 8. The mutual inductances between each side of the primary-side coils and the receiving coil L_s are, respectively, expressed as

$$\begin{aligned}M_{l_{a3}L_s}&=\frac{\mu_0 l_6 n_{w1} n_{w4}}{4\pi(\theta_8-\theta_7)}\ln\frac{|B_1J|}{|B_1F|}\\&\quad\times\int_{\theta_7}^{\theta_8}\left(\cos\theta+\cos\left(\tan^{-1}\frac{x}{l_{a3}-\frac{x}{\tan\theta}}\right)\right)\mathrm{d}\theta\\M_{l_{b1}L_s}&=-\frac{\mu_0 l_6 n_{w2} n_{w4}}{4\pi(\theta_4-\theta_3)}\ln\frac{|A_2J|}{|A_2F|}\\&\quad\times\int_{\theta_3}^{\theta_4}\left(\cos\theta+\cos\left(\tan^{-1}\frac{x}{l_{b1}-\frac{x}{\tan\theta}}\right)\right)\mathrm{d}\theta\\M_{l_{b3}L_s}&=-\frac{\mu_0 l_6 n_{w2} n_{w4}}{4\pi(\theta_6-\theta_5)}\ln\frac{|B_2J|}{|B_2F|}\\&\quad\times\int_{\theta_5}^{\theta_6}\left(\cos\theta+\cos\left(\tan^{-1}\frac{x}{l_{b3}-\frac{x}{\tan\theta}}\right)\right)\mathrm{d}\theta\\M_{l_{a4}L_s}&=-\frac{\mu_0 l_6 n_{w1} n_{w4}}{4\pi(\theta_{10}-\theta_9)}\ln\frac{|D_1G|}{|D_1F|}\\&\quad\times\int_{\theta_9}^{\theta_{10}}\left(\cos\theta+\cos\left(\tan^{-1}\frac{x}{l_{a4}-\frac{x}{\tan\theta}}\right)\right)\mathrm{d}\theta\\M_{l_{a2}L_s}&=-\frac{\mu_0 l_6 n_{w1} n_{w4}}{4\pi(\theta_{16}-\theta_{15})}\ln\frac{|A_1G|}{|A_1F|}\\&\quad\times\int_{\theta_{15}}^{\theta_{16}}\left(\cos\theta+\cos\left(\tan^{-1}\frac{x}{l_{a2}-\frac{x}{\tan\theta}}\right)\right)\mathrm{d}\theta\\M_{l_{b4}L_s}&=\frac{\mu_0 l_6 n_{w2} n_{w4}}{4\pi(\theta_{12}-\theta_{11})}\ln\frac{|D_2G|}{|D_2F|}\\&\quad\times\int_{\theta_{11}}^{\theta_{12}}\left(\cos\theta+\cos\left(\tan^{-1}\frac{x}{l_{b4}-\frac{x}{\tan\theta}}\right)\right)\mathrm{d}\theta\\M_{l_{b2}L_s}&=\frac{\mu_0 l_6 n_{w2} n_{w4}}{4\pi(\theta_{14}-\theta_{13})}\ln\frac{|A_2G|}{|A_2F|}\\&\quad\times\int_{\theta_{13}}^{\theta_{14}}\left(\cos\theta+\cos\left(\tan^{-1}\frac{x}{l_{b2}-\frac{x}{\tan\theta}}\right)\right)\mathrm{d}\theta.\end{aligned} \tag{14}$$

Therefore, the mutual inductance M_1 between the receiving coil and the transmitting coil and the mutual inductance M_2 between the receiving coil and the integrated reverse coil are expressed as

$$\begin{aligned}M_1&=M_{L_{a1}L_s}+M_{L_{a2}L_s}+M_{L_{a3}L_s}+M_{L_{a4}L_s}\\M_2&=M_{L_{b1}L_s}+M_{L_{b2}L_s}+M_{L_{b3}L_s}+M_{L_{b4}L_s}.\end{aligned} \tag{15}$$

To express the characteristics of the equivalent mutual inductance more intuitively, the corresponding mutual inductances are combined as follows:

$$\begin{aligned} M_{\mathrm{e}} &= M_1 + M_2 \\ &= (M_{L_{\mathrm{a1}}L_{\mathrm{s}}} + M_{L_{\mathrm{b1}}L_{\mathrm{s}}}) + (M_{L_{\mathrm{a2}}L_{\mathrm{s}}} + M_{L_{\mathrm{b2}}L_{\mathrm{s}}}) \\ &\quad + (M_{L_{\mathrm{a3}}L_{\mathrm{s}}} + M_{L_{\mathrm{b3}}L_{\mathrm{s}}}) + (M_{L_{\mathrm{a4}}L_{\mathrm{s}}} + M_{L_{\mathrm{b4}}L_{\mathrm{s}}}). \end{aligned} \tag{16}$$

In each item, the mutual inductances generated by the transmitting coil and the integrated reverse coil are included, whose directions are opposite. In addition, the following equations can be obtained based on (13), (14), and Fig. 8.

$$\begin{aligned} &\frac{|A_1J|}{|A_1F|} > \frac{|A_2J|}{|A_2F|}, \frac{|B_1J|}{|B_1F|} > \frac{|B_2J|}{|B_2F|} \\ &\frac{|A_1G|}{|A_1F|} > \frac{|A_2G|}{|A_2F|}, \frac{|D_1G|}{|D_1F|} > \frac{|D_2G|}{|D_2F|} \\ &\theta_2 - \theta_1 < \theta_4 - \theta_3, \theta_8 - \theta_7 < \theta_6 - \theta_5 \\ &\theta_{16} - \theta_{15} < \theta_{14} - \theta_{13}, \theta_{10} - \theta_9 < \theta_{12} - \theta_{11}. \end{aligned} \tag{17}$$

According to (16) and (17), the integrated reverse coil effectively converts the original single mutual inductance into an equivalent mutual inductance difference, thereby improving the anti-misalignment performance.

Based on the qualitative analysis of the mutual inductance expression under misalignment comprehensively considered in (13) and (14), two features are revealed as follows.

1) Compared to the transmitting coil, the integrated reverse coil has a smaller side length. Therefore, to make the variation of M_{p1s} and M_{p2s} under misalignment more similar, the turns of the integrated reverse coil are expected to be more than that of the transmitting coil. And more significant turns can make the variation rule of M_{p2s} closer to M_{p1s}, thereby making the total equivalent mutual inductance M_{ps} more stable. However, because the parameter of turns brings the gain of the overall mutual inductance value, its contribution to stability is limited. In addition, larger turns also result in more mutual inductance sacrifice.
2) A smaller side length can increase the impact of misalignment distance on M_{p2s} attenuation. Furthermore, the side length parameter is directly included in the factor containing misalignment distance in the (13), thus it can more effectively change the variation rule of M_{p2s}. It is the main determining factor for the stability of the total equivalent mutual inductance.

Therefore, to achieve better mutual inductance stability with smaller mutual inductance cancellation, reducing the geometric size of the integrated reverse coil under the same turns is an effective solution. The most practical method to achieve this is to increase the layers of the coil. Considering that excessive layers could increase the difficulty of coil design and bring serious heat dissipation issues, a double-layer integrated reverse coil is adopted in this article, as shown in Fig. 9.

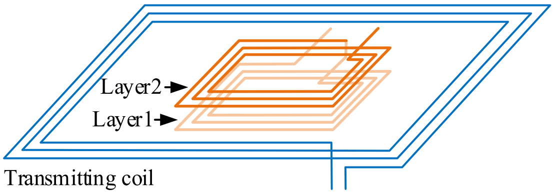

Fig. 9. Double-layer integrated reverse coil structure.

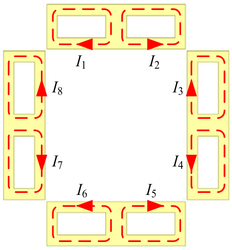

Fig. 10. Design of the primary-side integrated inductor coil.

Overall, compared to the turns parameter, the side length parameter is more effective in changing the variation rule of mutual inductance with misalignment distance *x*. The turns and size can be used as coarse and fine parameters to realize the stability of the mutual inductance. Within the range of turns slightly larger than the turns of the transmitting coil, the mutual inductance variation rules corresponding to different integrated reverse coil side lengths are expected to cover the initial main mutual inductance variation rule. Therefore, geometric dimensions can be optimized to make the variation of M_{p1s} and M_{p2s} under misalignment more similar. Therefore, the design idea is to optimize the size parameters under different fixed turns.

In addition, focusing on improving the compactness of the coupler, the inductor in the primary-side *LCC* resonance network is achieved by a coupling coil without affecting the system characteristics. The decoupling compensation inductor method utilizes four current loops, which can achieve decoupling with a unipolar coil under a multidirectional misalignment. The primary-side integrated inductor coil is designed as a special bipolar coil considering the adaptability to the misalignment of the *x*-direction and the *y*-direction, as shown in Fig. 10. Unlike the usual bipolar structure, the bipolar coil proposed in this article has eight current loops. Among them, two adjacent current loops have the opposite polarity. The transmitting coil and the integrated reverse coil are unipolar. Due to the central symmetry, the primary-side integrated inductor coil naturally decouples from them, even if misaligned both in the *x* and *y* directions.

IV. DESIGN OF THE MAGNETIC COUPLER

With the derived formula in Section II and the analysis in Section III, the HI magnetic coupler can be easily designed. The magnetic coupler structure is shown in Fig. 11. The parameters describing the coupler dimensions are defined in Table I.

In practical applications, the sizes of the transmitting coil and the receiving coil are subject to various restrictions based on the purpose, environment, and structure. Therefore, the parameters of the initial coupler are selected considering the required 3-kW experimental prototype. At the transmitter, the size of

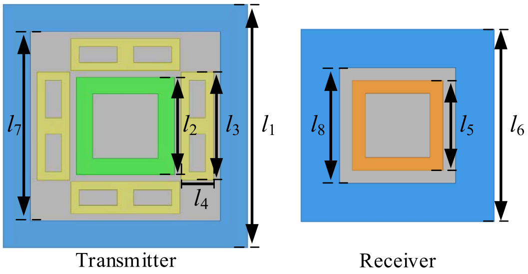

Fig. 11. HI magnetic coupler structure.

TABLE I
PARAMETERS OF THE MAGNETIC COUPLER

Type	Parameter	Description
Initial parameters	l_1	Outer length of L_{p1}
	l_6	Outer length of L_s
	l_7	Inner length of L_{p1}
	l_8	Inner length of L_s
	n_{w1}	Turns of L_{p1}
	n_{w4}	Turns of L_s
	x	Misalignment distance
	d	Transfer distance
Optimization parameters	l_2	Outer length of L_{p2}
	l_3	Outer length of $L_{pfi}(i=1,2,3,4)$
	l_4	Outer width of $L_{pfi}(i=1,2,3,4)$
	l_5	Outer length of L_{sf}
	n_{w2}	Turns of L_{p2}
	n_{w3}	Turns of $L_{pfi}(i=1,2,3,4)$
	n_{w5}	Turns of L_{sf}

the transmitting coil is designed as “450 mm $*$ 450 mm $*$ 5 mm.” The turns n_{w1} are designed as 10. At the receiver, the size of the receiving coil is designed as “300 mm $*$ 300 mm $*$ 5 mm.” The turns n_{w4} are designed as 12. The ferrite plate and aluminum shield of the same size with coils are used on both sides for magnetic field enhancement and electromagnetic shielding, respectively. The transfer distance is $d = 150$ mm.

Fig. 12 shows the flowchart for the design process of the magnetic coupler. The program starts with the analysis of the original mutual inductance under misalignment based on the initial parameters. And the design of the three integrated coils is performed in sequence. For the integrated reverse coil, the performance of the design result is evaluated by the standard deviation σ of equivalent mutual inductance M_{ps}. A smaller σ means a smaller fluctuation of the equivalent mutual inductance under misalignment, which reflects better misalignment tolerance. Therefore, the optimization goal is to obtain the key parameter turns and size corresponding to the minimum σ under misalignment. For the secondary-side integrated coil, the side length l_5 and turns n_{w5} are optimized based on the design goal of realizing the standard parameter L_{sfed} corresponding to the system power level. Then confirm whether ε obtained from the design results is less than 0.1 under well-aligned and misaligned. For the primary-side integrated inductor coil, the decoupling requirements were already met at the structural level and so the side length l_4 and turns n_{w3} are optimized to achieve the standard values L_{pfd} corresponding to the system power level.

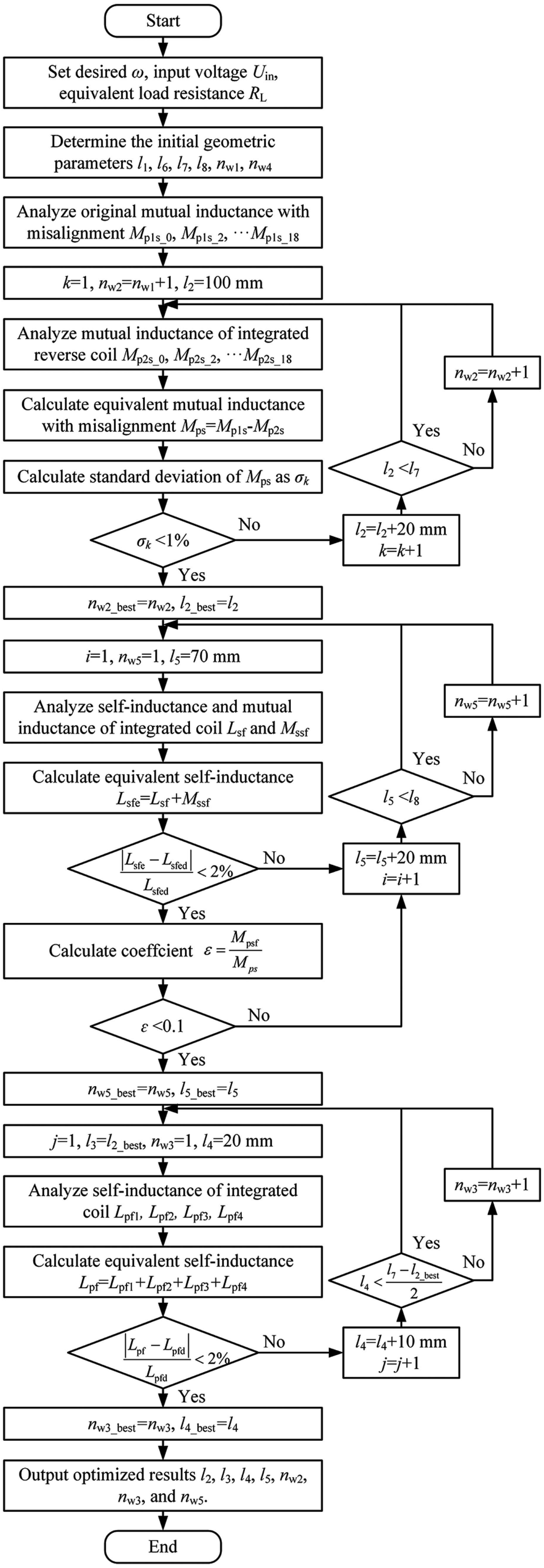

Fig. 12. Flowchart for the design process of the HI magnetic coupler.

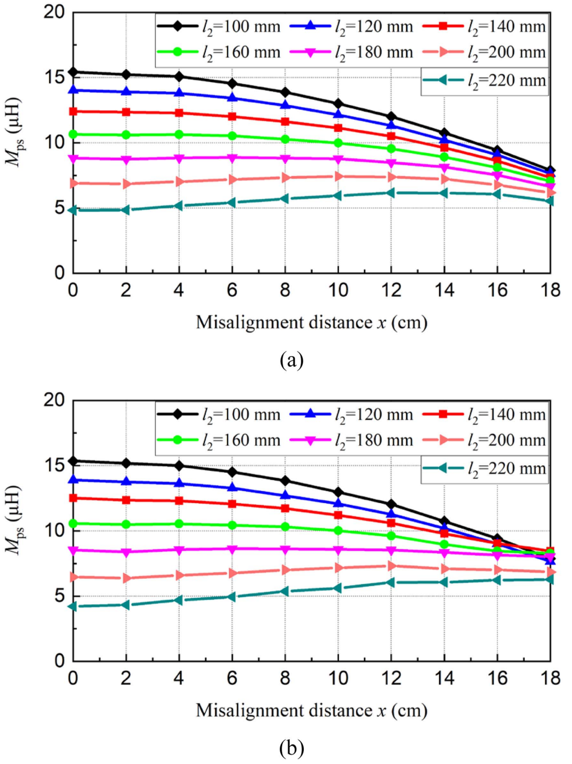

(a)

(b)

Fig. 13. Variation of the equivalent mutual inductance difference M_{ps} under misalignment with different lengths. (a) Case 1: $n_{\mathrm{w2}} = 11$. (b) Case 2: $n_{\mathrm{w2}} = 12$.

During the design process, reference indicators represent the performance and accuracy of optimization. The standard deviation of mutual inductance difference (2%) represents the degree of output power fluctuation under misalignment. Deviation of self-inductance parameters (2%) means the error range between the designed and the target parameters. And ε Less than 0.1 represents a weakly inductive resonant state.

Based on the analysis in Section III, the initial value of the turns n_{w2} of the integrated reverse coil is set to $n_{\mathrm{w1}}+1$. The design result corresponding to $n_{\mathrm{w2}} = 11$ and $n_{\mathrm{w2}} = 12$ is shown in Fig. 13. In Fig. 13(a), although the equivalent mutual inductance fluctuation under misalignment has been alleviated, it still cannot meet the target requirement of 2%. In Fig. 13(b), with the increase of l_2, the mutual inductance difference under misalignment increases more obviously compared to the well-aligned case. When $l_2 = 200$ mm and $l_2 = 220$ mm, the mutual inductance difference under misalignment even exceeds a well-aligned condition. When $l_2 = 180$ mm, the mutual inductance difference remains stable from well-aligned to 40% misalignment, which achieves the design goal. The IPT system using this mutual inductance difference for power transfer has excellent misalignment performance. Fig. 14 further shows the coupling characteristics of M_{p1s} and M_{p2s} when $l_2 = 180$ mm. The results show that the mutual inductance cancellation brought by the integrated reverse coil with a double-layer design is 51% of the original mutual inductance. Therefore, the size of the integrated reverse coil is designed as "180 mm $*$ 180 mm $*$ 5 mm." And the turns are designed as 12.

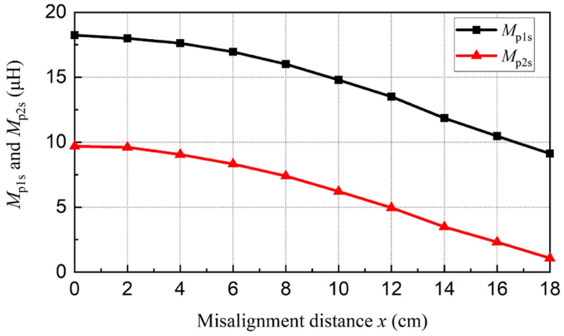

Fig. 14. Coupling characteristics of M_{p1s} and M_{p2s} when $l_2 = 180$ mm.

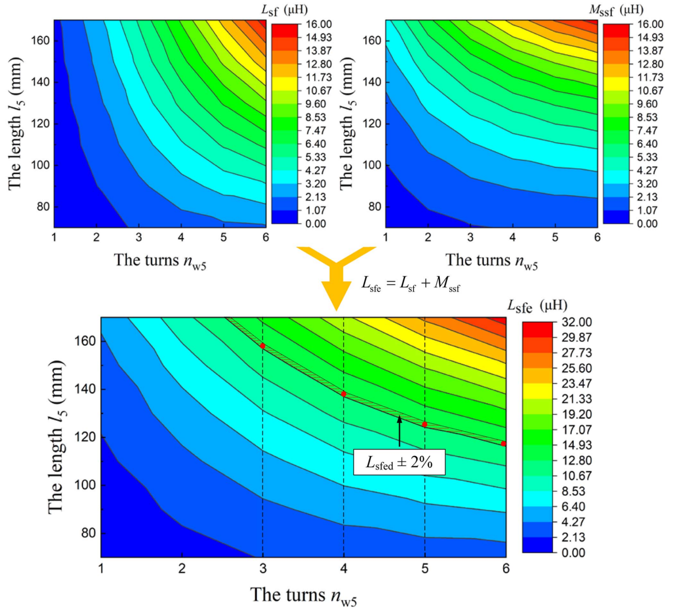

Fig. 15. Design result of the equivalent inductance L_{sfe} of the secondary-side integrated inductor coil affected by the turns n_{w5} and length l_5.

With the integrated reverse coil determined, the secondary-side integrated inductor coil is further designed to optimize the ZVS working condition and make the coupler more compact. According to the design process, the first step is to determine the selection range of size and turns based on the power level of the prototype. For the 3-kW output power level, the standard value of the secondary-side equivalent compensation inductance L_{sfed} is set to 11 μH. According to Fig. 3, the equivalent inductor in the secondary-side resonant network of the IPT system is L_{sfe}, which is the superposition of L_{sf} and M_{ssf}. Therefore, the crucial design of the secondary-side integrated inductor coil lies in the requirements of L_{sf} and M_{ssf}. Focusing on the optimization design of n_{w5} and l_5, the optimization results of the equivalent inductance L_{sfe} are shown in Fig. 15, where the shaded areas represent the target value L_{sfed}. According to the design process, the first obtained turns and size results are 3 and 160 mm, respectively. But in this situation, the calculated ε exceeds 0.1, which cannot meet the design demand. Continuing with $n_{\mathrm{w5}} = 4$ and $l_5 = 140$ mm, the variations of M_{psf}, M_{ps}, and their ratio

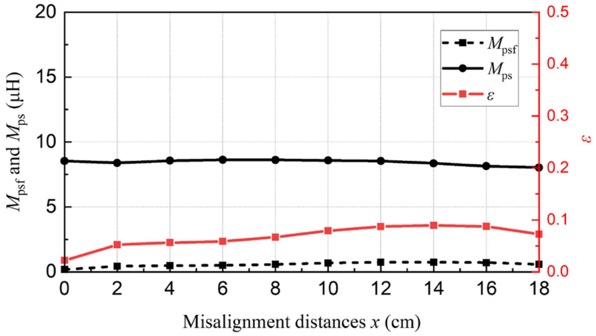

Fig. 16. Variation of M_{psf}, M_{ps}, and ε under different misalignment conditions.

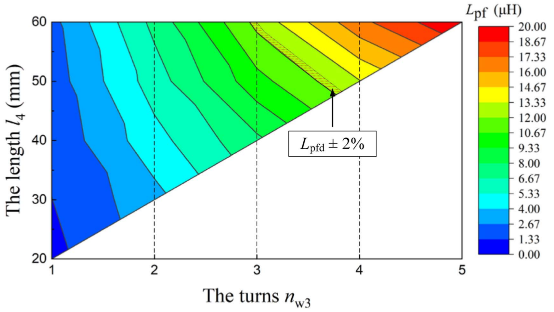

Fig. 17. Optimization result of L_{pf}.

ε when misaligned are shown in Fig. 16. The result shows that ε changes under misaligned conditions, but it maintains between the minimum value of 0 and the maximum value of 0.1, benefiting from M_{psf} being sufficiently small relative to M_{ps}. It not only can ensure the ZVS working condition but can also make the shutdown current not too large. Therefore, the size of the secondary-side integrated inductor coil is designed as "140 mm $*$ 140 mm $*$5 mm." The turns n_{w5} are designed as 4.

Considering the space utilization of the primary-side coupler, the length l_3 of the integrated compensation inductor coil is designed as 200 mm. And then the selection range of size and the turns are determined based on the power level. For the 3-kW output power level, the standard value of the primary-side equivalent compensation inductance L_{pfd} is set to 12.5 μH. Therefore, focusing on the optimization design of n_{w3} and l_4, the optimization results of L_{pf} are presented by the contour color temperature map in Fig. 17. The shaded areas represent the target value L_{pfd}. Obviously, the design results of turns n_{w3} and size l_4 are 3 and 60 mm, respectively. In summary, the size of the primary-side integrated coil is designed as "200 mm $*$60 mm $*$ 5 mm." The turns n_{w3} are designed as 3.

V. EXPERIMENTAL DETAILS

A. Verification Experiment

To verify the results of theoretical analysis and design methods, the experimental coils wound according to the design results in Section III are shown in Fig. 18. The overall experimental prototype is constructed as shown in Fig. 19. Consistent with the simulation, the transmission distance is set to 150 mm.

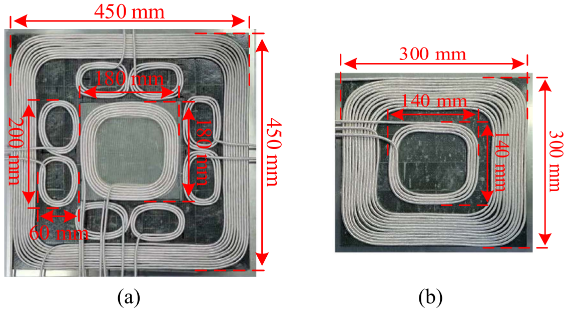

(a) (b)

Fig. 18. Prototype of the HI magnetic coupler. (a) Transmitting coil L_{p1} and integrated coils $L_{\mathrm{p2}}, L_{\mathrm{pf1}}, L_{\mathrm{pf2}}, L_{\mathrm{pf3}}, L_{\mathrm{pf4}}$. (b) Receiving coil L_{s} and integrated inductor coil L_{sf}.

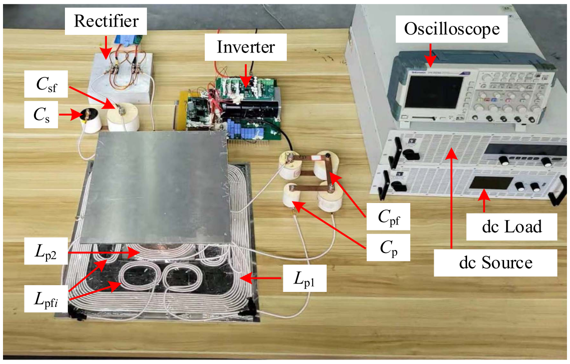

Fig. 19. Prototype of the IPT system with the HI magnetic coupler.

At the input, a dc source and a high-power inverter are used to provide a 300 V ac excitation for the resonant circuit. CREE silicon-carbide MOSFETs (C2M0025120D) with 25 mΩ internal resistance are adopted by the inverter to reduce power loss and improve output stability. The pulsewidth modulation control signal for the MOSFET is generated by the control chip TMS320F28335. The output is a fixed frequency of 85 kHz. At the output, CREE C3D20060D diodes are used for the rectifier to provide dc current to the EA-CPS-8080 electronic load. The electronic load is set to constant resistance mode with a resistance value of 30 Ω to meet the requirements of an output voltage of 300 V and an output current of 10 A. The coils are made from 1000-strand AWG 38 Litz-wire. The magnetic material PC95 is used to construct the ferrite board.

The measured parameters of the coupler and the calculated resonance parameters are given in Table II. The mutual inductance between the primary-side integrated inductor coil and the receiving coil under different misalignment conditions obtained from experimental measurements is shown in Fig. 20. The result shows that the mutual inductance between the integrated inductor coil and the receiving coil is within 0.04 μH in the entire misalignment area. Compared to other mutual inductances in the circuit, it is small enough to be neglected. In addition, M_{pfsf} is an extremely small value compared to M_{pfs}, as the self-inductance value of the integrated inductor coil on the secondary side is much smaller than that of the receiving coil. Therefore, the primary-side integrated inductor coil can achieve approximate

TABLE II
MEASURED PARAMETERS OF THE MAGNETIC COUPLER

Symbol	Parameters	Values
f	Resonant frequency	85 kHz
L_{p1}	Transmitting coil inductance	124.1 μH
L_{p2}	Integrated reverse coil inductance	65.9 μH
L_{pf1}	Primary-side integrated inducance	3.5 μH
L_{pf2}	Primary-side integrated inducance	3.4 μH
L_{pf3}	Primary-side integrated inducance	3.4 μH
L_{pf4}	Primary-side integrated inducance	3.2 μH
L_{s}	Receiving coil inductance	92.3 μH
L_{sf}	Secondary-side integrated inductance	7.5 μH
C_{p}	Primary-side compensate capacitor	24.1 nF
C_{pf}	Primary-side compensate capacitor	262.3 nF
C_{s}	Secondary-side compensate capacitor	44.4 nF
C_{sf}	Secondary-side compensate capacitor	500.0 nF

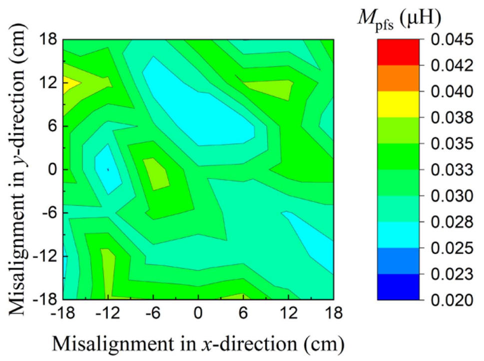

Fig. 20. Mutual inductance M_{pfs} under different misalignment conditions.

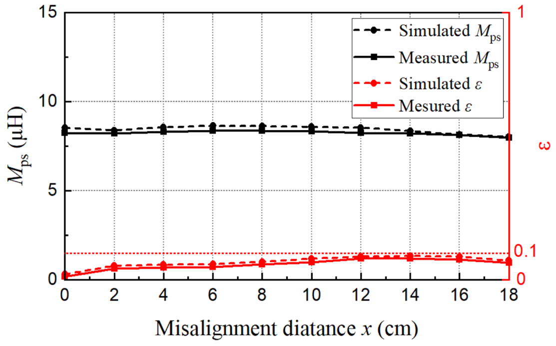

Fig. 21. Comparison of experimental and simulated values of M_{ps} and ε.

decoupling compatible with multidirectional misalignment conditions.

The experimental measurement values of M_{ps} and ε are compared with the theoretical values, as shown in Fig. 21. The result shows that the theoretical and experimental results are very close, and the trend of parameter variations is consistent. The mutual inductance difference M_{ps} remains stable within the 18 cm misaligned range, with a fluctuation of ± 2% in its square value, achieving suppression of output power fluctuation during misalignment. In addition, the actual measured value of ε is close to the simulation results, which meets the optimized configuration of ZVS conditions.

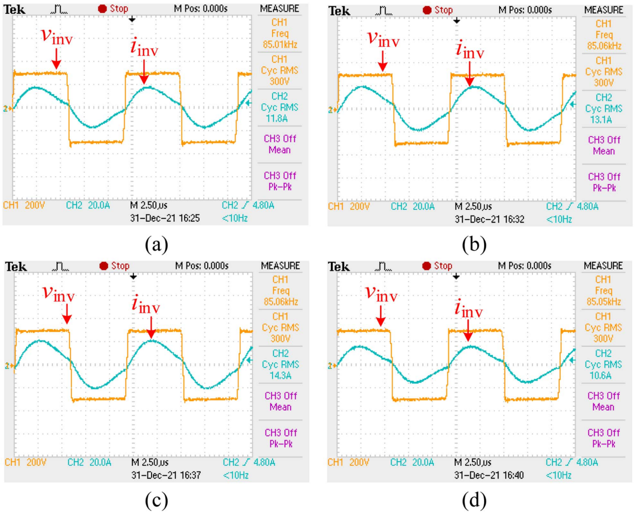

(a) (b)
(c) (d)

Fig. 22. Steady waveforms of the voltages and currents of the inverter. (a) $x = 0$ cm. (b) $x = 6$ cm. (c) $x = 12$ cm. (d) $x = 18$ cm.

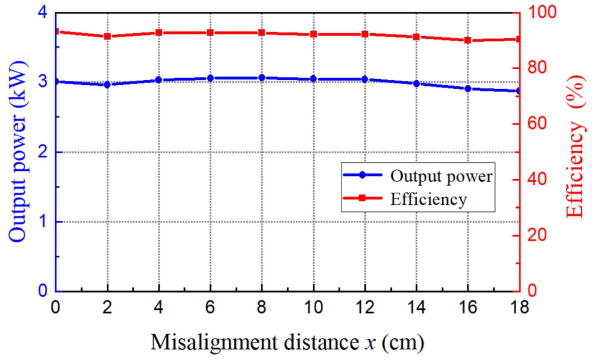

Fig. 23. System output power and efficiency under misalignment.

The inverter output waveforms of the system under different misalignment distances are shown in Fig. 22. v_{inv} is the inverter voltage and i_{inv} is the inverter current. The experiment proves that the system works efficiently under well-aligned and different misalignment conditions. And the inverter keeps working in an ideal weak inductive state, and the integrated coil on the secondary side effectively optimizes the ZVS condition.

The output power and dc–dc overall system efficiency of the IPT system against misalignment at $R_L = 30\ \Omega$ are given in Fig. 23. Within the misalignment range of 18 cm, the output power ranges from 2.9 to 3.1 kW. The average output power is 3 kW. Under the working condition of 18 cm misalignment, the output power is reduced to 2.9 kW, which is 97% of the well-aligned value (3.1 kW). The overall efficiency of the IPT system reaches 93.1%. The results validate that the proposed method has good misalignment tolerance.

The performance of the proposed highly magnetic integrated method is compared with the conventional and partially integrated *LCC* compensation systems, respectively. The integrated reverse coil is removed and integrated compensation inductors

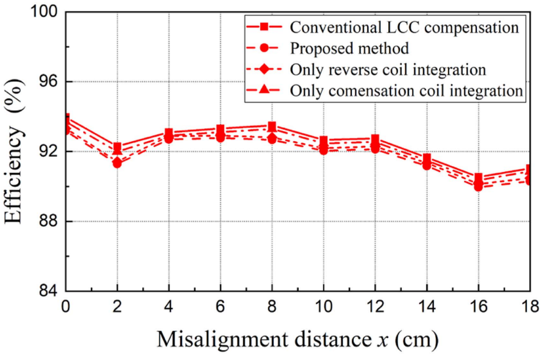

Fig. 24. Efficiency comparison between normal *LCC* compensation and the proposed method.

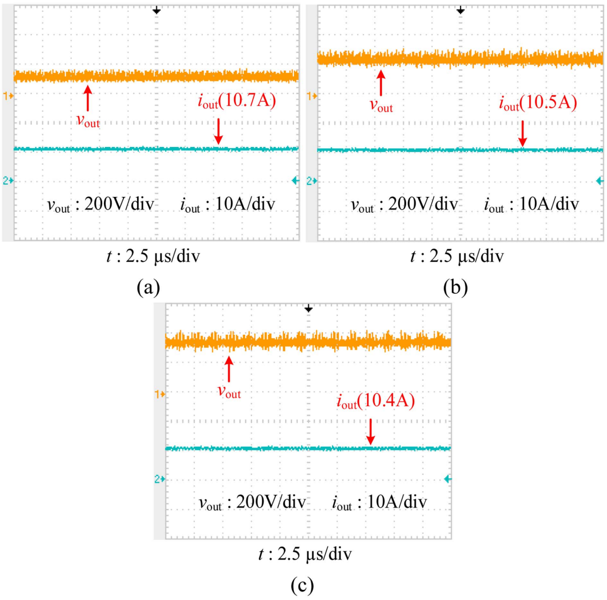

Fig. 25. Output voltage and current waveforms under misalignment with different loads. (a) $x = 0$ cm, $R_L = 10\ \Omega$. (b) $x = 9$ cm, $R_L = 20\ \Omega$. (c) $x = 18$ cm, $R_L = 30\ \Omega$.

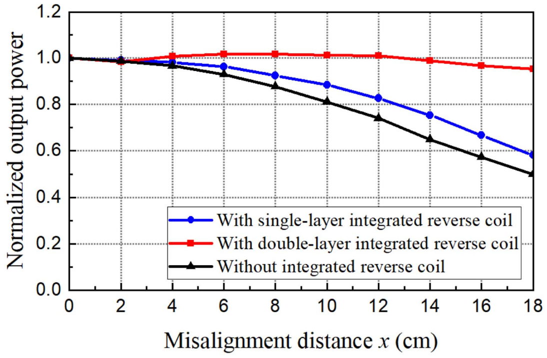

Fig. 26. Comparison of output power fluctuation under misalignment.

are replaced by external inductors to form the conventional *LCC*-compensated system. And two partially magnetic integrated *LCC* compensation systems are formed by integrating only the reverse coil or only the compensation inductor coil. The comparison results of the dc–dc efficiency of these systems are shown in Fig. 24. The efficiency of the proposed system is slightly lower than the normal system, mainly caused by the more copper used by the reverse coil. Due to the coupling effect of the double-layer reverse coil and the internal mutual inductance effect of the integrated compensation inductor coil on the secondary side, the average efficiency difference under misalignment is within 1%. It is worthwhile to sacrifice such less efficiency for excellent misalignment tolerance and compactness.

B. Comparison Experiment

To verify the constant current output characteristics of the system and the superiority of the double-layer reverse coil, two sets of comparative experiments were performed separately.

The experiment is conducted with load resistances of 10 Ω, 20 Ω, and 30 Ω under typical misaligned conditions, respectively. Fig. 25 shows the output current and voltage results under different load resistances. The result shows that the proposed system has constant current output characteristics throughout the entire working state.

In addition, a single-layer integrated reverse coil with half turns was used as a comparative experiment, while a system without reverse coils was used as a comparison. Based on the theoretical analysis in Section II, the experimental parameters are consistent with those of the double-layer integrated coil system. The comparison of the variations in output power under misalignment is shown in Fig. 26. Fig. 26 shows that the output power of the proposed design has a good misalignment tolerance. The output power can remain approximately constant during 18-cm misalignment, while it changes significantly due to the decline of mutual inductance in the system without the reverse coil. In addition, compared with the single-layer integrated reverse coil system, the proposed double-layer structure has better mutual inductance shaping ability under the same geometric size. Therefore, the performance of the proposed design is better, especially in smaller mutual inductance cancellations. The double-layer coil design realizes output power stability at 40% misalignment with only 51% mutual inductance cancellation.

VI. DISCUSSION

The integrated reverse coil on the primary side is used to partly cancel the primary mutual inductance to achieve stability, thereby reducing the output power capability of the IPT system. By analyzing the coupling characteristics of the integrated reverse coil, the relationship between the variation rule of total equivalent mutual inductance under misalignment and its geometric size is clarified. Better magnetic field shaping is realized by the proposed double-layer integrated reverse coil. The comparison between this article with the latest related research is given in Table III. The proposed method is useful in improving misalignment tolerance, compactness, ZVS working condition, and efficiency performance, with the cancellation of mutual

TABLE III
COMPARISON BETWEEN THE LATEST RELATED RESEARCH AND THIS WORK

Integrated Method	Maximum Efficiency	Output Power	Misalignment Tolerance	Integration Degree	ZVS Design	Mutual Inductance Cancellation Ratio
[6]	\	1.9 kW	\	\	No	\
[11]	95.1%	1 kW	25% (20 cm/80 cm)	\	No	\
[13]	91.1%	3 kW	21% (16 cm/74 cm)	Low	No	\
[14]	92.5%	1 kW	25% (10 cm/40 cm)	Low	No	\
[28]	92.1%	3.4 kW	35% (16 cm/45 cm)	Low	No	75%
[29]	90.7%	0.22 kW	25% (10 cm/40 cm)	Low	No	70%
[31]	91.1%	1 kW	35% (16 cm/45 cm)	Low	No	76%
[This Work]	93.1%	3 kW	40% (18 cm/45 cm)	High	Yes	51%

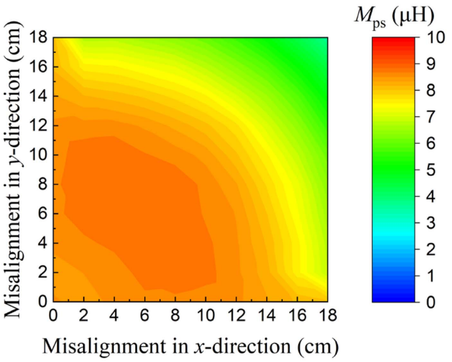

Fig. 27. Simulated M_{ps} under both the *x* and *y* directions of misalignments.

inductance reduced. The double-layer coil design effectively restricts the shaping of the magnetic field, achieving output power stability at 40% misalignment with only 51% mutual inductance cancellation.

To further explore the performance of the proposed system with simultaneous misalignment in the *x* and *y* directions, the simulated mutual inductance M_{ps} under both the *x* and *y* directions of misalignments is shown in Fig. 27. The result shows that while maintaining a smaller mutual inductance cancellation, the equivalent mutual inductance used for power transmission still has a certain stable effect simultaneously misaligned within a certain range both in the *x* and *y* directions.

In addition, the secondary-side integrated inductor is beneficial for improving the output power capability. The internal coupling between the secondary-side integrated compensation inductor coil and the receiving coil reduces the compensation inductor value under the same output power requirements. Therefore, it is possible to improve the output power capability of the system by reducing the demand for secondary-side compensation inductor values under the limit of the current withstand. The original adverse effects of integrated reverse coils have been mitigated.

VII. CONCLUSION

In this article, a highly magnetic integrated method of *LCC*-compensated IPT system is proposed in which coupling coils are integrated into the coupler to improve the misalignment tolerance and realize the design of ZVS condition. All the inductor components in the *LCC* resonant network are integrated into the magnetic coupler, and the coil in reverse series with the transmitting coil is integrated into the transmitter. The system's antimisalignment performance, ZVS conditions, and compact have been optimized and improved. And output power stability under misalignment with fewer mutual inductance cancel sacrifices is realized. Theoretical calculations and qualitative magnetic field analysis are performed to reveal the working principle and design criteria of the integrated coils. A 3-kW prototype has been built to verify the theoretical analysis and design method. Experiments show that the proposed magnetic integration method will effectively optimize the ZVS condition, maintaining 97% of the standard output power at a misalignment distance of 40% relative to the side length of the transmitting coil. The mutual inductance cancellation caused by the reverse coil is reduced to 51%, and the efficiency reaches 93.1%.

REFERENCES

[1] C. Liu, C. Jiang, J. Song, and K. T. Chau, "An effective sandwiched wireless power transfer system for charging implantable cardiac pacemaker," *IEEE Trans. Ind. Electron.*, vol. 66, no. 5, pp. 4108–4117, May 2019.

[2] T.-D. Yeo, D. Kwon, S.-T. Khang, and J.-W. Yu, "Design of maximum efficiency tracking control scheme for closed-loop wireless power charging system employing series resonant tank," *IEEE Trans. Power Electron.*, vol. 32, no. 1, pp. 471–478, Jan. 2017.

[3] Y. Liu, U. K. Madawala, R. Mai, and Z. He, "Zero-phase-angle controlled bidirectional wireless EV charging systems for large coil misalignments," *IEEE Trans. Power Electron.*, vol. 35, no. 5, pp. 5343–5353, May 2020.

[4] S. Li, L. Wang, Y. Guo, C. Tao, and L. Ji, "Power stabilization with double transmitting coils and T-type compensation network for dynamic wireless charging of EV," *IEEE J. Emerg. Sel. Topics Power Electron.*, vol. 8, no. 2, pp. 1801–1812, Jun. 2020.

[5] K. Song et al., "A control strategy for wireless EV charging system to improve weak coupling output based on variable inductor and capacitor," *IEEE Trans. Power Electron.*, vol. 37, no. 10, pp. 12853–12864, Oct. 2022.

[6] M. Budhia, J. T. Boys, G. A. Covic, and C.-Y. Huang, "Development of a single-sided flux magnetic coupler for electric vehicle IPT charging systems," *IEEE Trans. Ind. Electron.*, vol. 60, no. 1, pp. 318–328, Jan. 2013.

[7] K. Song et al., "Design of DD coil with high misalignment tolerance and low EMF emissions for wireless electric vehicle charging systems," *IEEE Trans. Power Electron.*, vol. 35, no. 9, pp. 9034–9045, Sep. 2020.

[8] J. Mai, Y. Wang, Y. Yao, M. Sun, and D. Xu, "High-misalignment-tolerant IPT systems with solenoid and double D pads," *IEEE Trans. Ind. Electron.*, vol. 69, no. 4, pp. 3527–3535, Apr. 2022.

[9] C. Xia, W. Wang, S. Ren, X. Wu, and Y. Sun, "Robust control for inductively coupled power transfer systems with coil misalignment," *IEEE Trans. Power Electron.*, vol. 33, no. 9, pp. 8110–8122, Sep. 2018.

[10] T.-S. Lee, S.-J. Huang, S.-H. Dai, and J.-L. Su, "Design of misalignment-insensitive inductive power transfer via interoperable coil module and dynamic power control," *IEEE Trans. Power Electron.*, vol. 35, no. 9, pp. 9024–9033, Sep. 2020.

[11] H. Feng, T. Cai, S. Duan, J. Zhao, X. Zhang, and C. Chen, "An LCC-compensated resonant converter optimized for robust reaction to large coupling variation in dynamic wireless power transfer," *IEEE Trans. Ind. Electron.*, vol. 63, no. 10, pp. 6591–6601, Oct. 2016.

[12] L. Zhao, D. J. Thrimawithana, and U. K. Madawala, "Hybrid bidirectional wireless EV charging system tolerant to pad misalignment," *IEEE Trans. Ind. Electron.*, vol. 64, no. 9, pp. 7079–7086, Sep. 2017.

[13] Y. Chen, B. Yang, Z. Kou, Z. He, G. Cao, and R. Mai, "Hybrid and reconfigurable IPT systems with high-misalignment tolerance for constant-current and constant-voltage battery charging," *IEEE Trans. Power Electron.*, vol. 33, no. 10, pp. 8259–8269, Oct. 2018.

[14] S. Li, W. Li, J. Deng, T. D. Nguyen, and C. C. Mi, "A double-sided LCC compensation network and its tuning method for wireless power transfer," *IEEE Trans. Veh. Technol.*, vol. 64, no. 6, pp. 2261–2273, Jun. 2015.

[15] W. Li, H. Zhao, S. Li, J. Deng, T. Kan, and C. C. Mi, "Integrated LCC compensation topology for wireless charger in electric and plug-in electric vehicles," *IEEE Trans. Ind. Electron.*, vol. 62, no. 7, pp. 4215–4225, Jul. 2015.

[16] T. Kan, T.-D. Nguyen, J. C. White, R. K. Malhan, and C. C. Mi, "A new integration method for an electric vehicle wireless charging system using LCC compensation topology: Analysis and design," *IEEE Trans. Power Electron.*, vol. 32, no. 2, pp. 1638–1650, Feb. 2017.

[17] T. Kan, F. Lu, T.-D. Nguyen, P. P. Mercier, and C. C. Mi, "Integrated coil design for EV wireless charging systems using LCC compensation topology," *IEEE Trans. Power Electron.*, vol. 33, no. 11, pp. 9231–9241, Nov. 2018.

[18] F. Lu, H. Zhang, H. Hofmann, W. Su, and C. C. Mi, "A dual-coupled LCC-compensated IPT system with a compact magnetic coupler," *IEEE Trans. Power Electron.*, vol. 33, no. 7, pp. 6391–6402, Jul. 2018.

[19] L. Zhao, D. J. Thrimawithana, U. K. Madawala, A. P. Hu, and C. C. Mi, "A misalignment-tolerant series-hybrid wireless EV charging system with integrated magnetics," *IEEE Trans. Power Electron.*, vol. 34, no. 2, pp. 1276–1285, Feb. 2019.

[20] K. Shi, C. Tang, H. Long, X. Lv, Z. Wang, and X. Li, "Power fluctuation suppression method for EV dynamic wireless charging system based on integrated magnetic coupler," *IEEE Trans. Power Electron.*, vol. 37, no. 1, pp. 1118–1131, Jan. 2022.

[21] K. Shi, C. Tang, Z. Wang, X. Li, Y. Zhou, and Y. Fei, "A magnetic integrated method suppressing power fluctuation for EV dynamic wireless charging system," *IEEE Trans. Power Electron.*, vol. 37, no. 6, pp. 7493–7503, Jun. 2022.

[22] W.-S. Lee, W.-I. Son, K.-S. Oh, and J.-W. Yu, "Contactless energy transfer systems using antiparallel resonant loops," *IEEE Trans. Ind. Electron.*, vol. 60, no. 1, pp. 350–359, Jan. 2013.

[23] W.-S. Lee, K.-S. Oh, and J.-W. Yu, "Distance-insensitive wireless power transfer and near-field communication using a current-controlled loop with a loaded capacitance," *IEEE Trans. Antennas Propag.*, vol. 62, no. 2, pp. 936–940, Feb. 2014.

[24] W.-S. Lee, K.-S. Oh, and J.-W. Yu, "Field analysis and measurement of antiparallel resonant loop for wireless charging," *IEEE Antennas Wireless Propag. Lett.*, vol. 14, pp. 1459–1462, 2015.

[25] S. Wang, Z. Hu, C. Rong, C. Lu, J. Chen, and M. Liu, "Planar multiple-antiparallel square transmitter for position-insensitive wireless power transfer," *IEEE Antennas Wireless Propag. Lett.*, vol. 17, no. 2, pp. 188–192, Feb. 2018.

[26] J. Kim, H. C. Son, and Y. J. Park, "Multi-loop coil supporting uniform mutual inductances for free-positioning WPT," *Electron. Lett.*, vol. 49, no. 6, pp. 417–419, Mar. 2013.

[27] Y. Chen, R. Mai, Y. Zhang, M. Li, and Z. He, "Improving misalignment tolerance for IPT system using a third-coil," *IEEE Trans. Power Electron.*, vol. 34, no. 4, pp. 3009–3013, Apr. 2019.

[28] Z. Dong, X. Li, S. Liu, Z. Xu, and L. Yang, "A novel all-direction anti-misalignment wireless power transfer system designed by truncated region eigenfunction expansion method," *IEEE Trans. Power Electron.*, vol. 36, no. 11, pp. 12456–12467, Nov. 2021.

[29] Y. Zhang, S. Chen, X. Li, and Y. Tang, "Design methodology of free-positioning nonoverlapping wireless charging for consumer electronics based on antiparallel windings," *IEEE Trans. Ind. Electron.*, vol. 69, no. 1, pp. 825–834, Jan. 2022.

[30] P. Zhang, M. Saeedifard, O. C. Onar, Q. Yang, and C. Cai, "A field enhancement integration design featuring misalignment tolerance for wireless EV charging using LCL topology," *IEEE Trans. Power Electron.*, vol. 36, no. 4, pp. 3852–3867, Apr. 2021.

Ke Shi received the B.E. degree in automation and the Ph.D. degree in control theory and control engineering from the School of Automation, Chongqing University, Chongqing, China, in 2016, and 2022, respectively.

He is currently a Lecturer with the School of Automation, Chongqing University of Posts and Telecommunications, Chongqing, China. His current research interests include wireless power transfer and power electronics, dynamic wireless charging systems, and magnetic integrated methods.

Tianxu Feng received the B.E. degree in automation and the Ph.D. degree in control theory and control engineering from the School of Automation, Chongqing University, Chongqing, China, in 2016, and 2022, respectively.

He is currently a Lecturer with the School of Automation, Chongqing University of Posts and Telecommunications, Chongqing, China. His current research interests include wireless power transfer and power electronics.

Jincheng Jiang received the Ph.D. degree in control theory and control engineering from the School of Automation, Chongqing University, Chongqing, China, in 2020.

He is currently a Lecturer with the School of Automation, Chongqing University of Posts and Telecommunications, Chongqing. His research interests include wireless power transfer technology and industrial IoT technology.

Peiyue Wang received the B.E. degree in automation from Xidian University, Xi'an, China, in 2015, and the Ph.D. degree in control theory and engineering from Chongqing University, Chongqing, China, in 2021.

He is currently a Lecturer with the School of Automation, Chongqing University of Posts and Telecommunications, Chongqing. His current research interests include wireless power transfer and power electronics.

Zhenya Meng received the M.D. degree in condensed matter physics from the School of Physics, Chongqing University, Chongqing, China, in 2015, and the Ph.D. degree in circuits and systems from the School of Microelectronics and Communication Engineering, Chongqing University, Chongqing, China, in 2020.

He is currently a Lecturer with the College of Automation, Chongqing University of Posts and Telecommunications, Chongqing, China. His current research interests include microwave wireless energy transmission, millimeter-wave antenna, and intelligent reflection surface.

Chunsen Tang (Member, IEEE) received the B.E. degree in automation and the Ph.D. degree in control theory and control engineering from the School of Automation, Chongqing University, Chongqing, China, in 2004 and 2009, respectively.

In 2008, he was a Research Fellow with the Department of Electrical and Computer Engineering, The University of Auckland, Auckland, New Zealand. In 2009, he joined the School of Automation, Chongqing University, where he is currently a Professor. His current research interests include nonlinear modeling and analysis, intelligent control, and wireless power transfer.